Reliable Drag Extraction from Numerical Solutions: Elimination of Spurious Drag

S. Esquieu
Research Scientist
Applied Aerodynamics Department
Civil Aircraft Unit
ONERA Meudon
8 rue des Vertugadins, F-92190 MEUDON, FRANCE

Sebastien.Esquieu@onera.fr

ABSTRACT

This paper focuses on the ability of the ONERA far-field drag extraction method to provide reliable drag prediction. The combination mesh discretization-quality / numerical schemes and truncation errors inherent to CFD-codes leads to spurious entropy productions within the flow-field. This error of the numerical approximation has an important impact on the prediction of drag. Indeed, the direct surface force integration, the near-field drag, given by aerodynamic codes cannot distinguish spurious contributions to drag from physical ones because the numerical error is implicitly contained in the aerodynamic variables used for the integral outputs. By field analysis, the far-field approach locates and separates the spurious drag productions from the physical ones. This is an asset of the method which largely reduces the dependency of the drag extraction results to the mesh quality and CFD computation accuracy. Thanks to this spurious drag elimination, the post-processing method provides reliable far-field drag breakdown into its physical components i.e. viscous drag, wave drag and lift-induced drag which represent very useful and instructive data for the aerodynamic designers.

NOMENCLATURE

M	Mach number
M_∞	freestream Mach number
x, y, z	orthogonal coordinate system; x is flight direction
ρ	density
u, v, w	velocity components in x, y, z-direction
u_∞	freestream velocity
p	static pressure
p_∞	freestream static pressure
$\vec{q}$	velocity vector
r	gas constant
γ	ratio of specific heats
$\vec{\tau}_x = [\tau_{xx}\tau_{xy}\tau_{xz}]^T$	vector of viscous stresses
$[\tau] = [\vec{\tau}_x\vec{\tau}_y\vec{\tau}_z]$	matrix of viscous stresses
Δs	variation of entropy relative to its freestream value
ΔH	variation of stagnation enthalpy relative to its freestream value

Esquieu, S. (2007) Reliable Drag Extraction from Numerical Solutions: Elimination of Spurious Drag. In *Computational Uncertainty in Military Vehicle Design* (pp. 42-1 – 42-16). Meeting Proceedings RTO-MP-AVT-147, Paper 42. Neuilly-sur-Seine, France: RTO. Available from: http://www.rto.nato.int.

$\vec{n}$	outward normal unit vector
Cp	pressure coefficient
D_p	pressure drag
D_f	friction drag
D_w	wave drag
D_v	viscous drag
D_{vp}	viscous pressure drag
D_i	induced (or vortex) drag
D_{sp}	spurious drag

1 INTRODUCTION

The predictive ability of Computational Fluid Dynamics (CFD) is of primary importance for aircraft design purposes, especially regarding the drag prediction which remains one of the major challenges in aerodynamics as indicated by Slooff [1]. Indeed, reliable drag evaluation requires good quality meshes and accurate numerical solutions because this component is very sensitive to numerical deviations.
In 1985, Rizzi [2] gave an excellent introduction to the subject by introducing the concept of spurious entropy productions and in 1990 van der Vooren and Slooff [3] presented a detailed theory of the far-field analysis method for an accurate drag prediction. Since 1990, ONERA has been developing original methods to determine drag from numerical solutions [4] and at present a new far-field drag extraction software (FFD72) allows, thanks to its face-based data structure, to extract drag as well from structured as from unstructured computations.
In CFD, an important discrepancy between the numerical and theoretical aspects of drag extraction is that spurious irreversible drag may be generated by the numerical technique used to solve the equations [5] leading to a poor evaluation of the drag components. Nevertheless, the far-field technique ensures more reliable drag prediction than the direct near-field method (surface integration of pressure and friction stresses) because of the detection and elimination of these spurious drag productions.
As indicated by Mendenhall and al. [6], at the moment different methods are used for the reduction of uncertainties in CFD. For example, recent efforts have been realized to quantify the effects of truncation errors on a CFD computation [7]. Papers are also devoted to intelligent solution-adaptative gridding via solutions of the adjoint equations [8] [9] to correct the aerodynamic flow variables to obtain more reliable integral outputs such as drag, lift and moment. Here, the purpose of this study is to ensure more reliable drag prediction than the direct surface integration only by a post-processing of the solution without modifying the computed flow-field.
The present work adresses the problem of the spurious drag separation and elimination thanks to the far-field analysis and its positive consequence on the drag prediction. For that, this paper starts with a short presentation of the far-field drag theory and methodology. Then, the subject of the localisation of the spurious drag productions within the flow-field is addressed and the effects of the numerical error on the pressure drag component are presented in detail in the context of two numerical examples: an inviscid calculation on the NACA 0012 airfoil and a Navier-Stokes calculation on the AS28 wing/body configuration. A second aspect concerns the spurious decay of the trailing vortices downstream of lifting finite surfaces on the AS28 wing-body configuration in multi-block structured and unstructured hybrid approches. All the results obtained are discussed in terms of drag prediction accuracy and reliability.

2 DRAG EXTRACTION FROM NUMERICAL SOLUTIONS

Drag can be extracted from a numerical flow solution either by surface integration (near-field approach) or through a field analysis (far-field method).

2.1 Near-field drag

The former technique is straightforward and available in all aerodynamics codes. It gives a mechanical breakdown of the drag into its normal (pressure) and tangential (friction) components.

The **near-field drag** can be expressed as:

$$D = D_p + D_f = \int_{S_A} [(p - p_\infty)n_x - (\vec{\tau_x}.\vec{n})]dS \tag{1}$$

where S_A is the aircraft surface as shown in figure 1 and $n_x = \vec{n}.\vec{i}$ with $\vec{i}$ the unit vector in the free-stream flow direction.

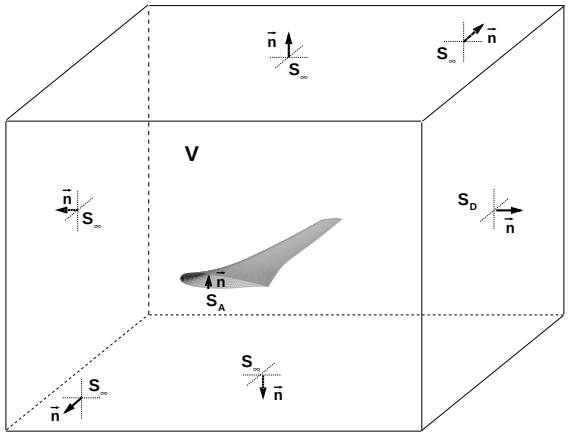

Figure 1: Control volume V.

The near-field approach is very efficient to determine the lift coefficient but is less reliable for the drag prediction because this component is very sensitive to numerical errors. For transonic aircraft configurations in cruise conditions, the lift coefficient represents between 15 and 25 times the drag coefficient and so it is easy to guess a higher sensitivity of the drag component to numerical effects than the lift coefficient.

The pressure drag component results from an imbalance between pressure forces acting in the drag direction ($C_p.n_x > 0$) and in suction forces acting in thrust direction ($C_p.n_x < 0$) (see figure 2). Generally the suction is under-estimated leading to an over-estimation of the pressure drag, Very small numerical deviations on the pressure distribution will have a very important impact on the pressure drag values. Thanks to the far-field approach, we will show in a next section the effects of numerical errors on this pressure component.

The skin-friction drag component results from the frictional shear stress exerted by the fluid on the surface of the body in the tangential direction. In the context of numerical uncertainty, we can add two important sources of error concerning the friction drag evaluation. In solving the RANS equations one of the models with the highest uncertainty is the turbulence model which affects not only the pressure drag but also and often more the friction drag component. Furthermore, the evaluation of this component is dependent on the way to compute the velocity gradients within the boundary layer and this can have a non-negligible impact on the friction drag prediction. These two important aspects for a reliable friction drag prediction are not addressed in this paper but are of primary importance.

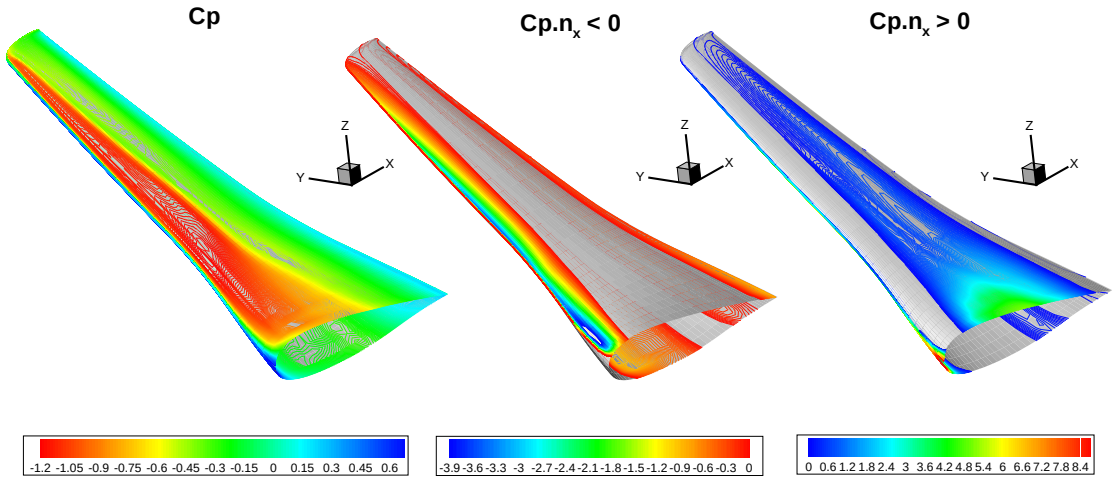

Figure 2: AS28 wing ($M = 0.80, \alpha = 2.2^o, Re_{/m} = 11.0\ 10^6$) - Pressure distribution and imbalance between pressure and suction forces.

2.2 Far-field drag

The ONERA method for far-field drag extraction from numerical solutions follows a formulation recently introduced by van der Vooren [4] and discussed by Destarac in [5].
This technique is based on a far-field analysis and the theoretical basis of the far-field drag computation and breakdown is the use of the momentum theorem and mass conservation (see detailed presentation in [5] [14]) which leads to the use and decomposition of vector $\vec{f}$:

$$\vec{f} = -\rho(u - u_\infty)\vec{q} - (p - p_\infty)\vec{i} + \vec{\tau_x} \tag{2}$$

With this theory, distinction must be made between thermodynamic irreversible process (viscous drag and wave drag production) and reversible process (induced drag production). By selecting zones in the field thanks to physical criteria [16], it may give a phenomenological breakdown of drag [18] into the physical drag sources: wave drag, viscous drag and lift-induced drag. The physical breakdown of drag is considered as more useful than the mechanical, by design engineers.
Field quantities involved in this far-field technique are based on a velocity defect $\Delta\overline{u}$ which can be written as:

$$\Delta\overline{u} = u_\infty \sqrt{1 + \frac{2\Delta H_i}{{q_\infty}^2} - \frac{2[(e^{\frac{\Delta s}{r}})^{(\frac{\gamma-1}{\gamma})} - 1]}{(\gamma - 1){M_\infty}^2}} - u_\infty \tag{3}$$

This formula expresses the velocity defect in a flow without trailing vorticity recovering freestream pressure downstream of the body. The variations of entropy Δs and stagnation enthalpy ΔH_i (see figure 3) come from thermodynamic irreversible phenomena generated within the shear layers (boundary layer and wake) and within the shocks.

2.2.1 Viscous and wave drag

Viscous and wave drag are due to irreversible phenomena which imply a change in energy form and so it is convenient to define the vector $\vec{f_{vw}}$ relative to the irreversible drag productions:

$$\vec{f_{vw}} = -\rho\Delta\overline{u}\vec{q} \tag{4}$$

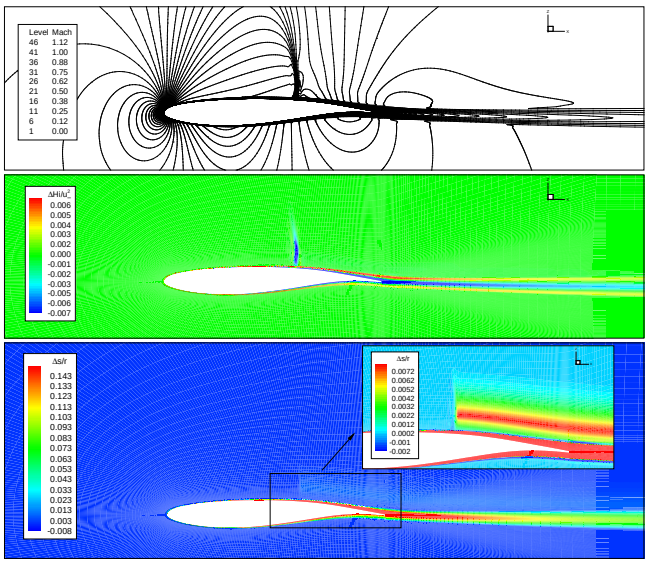

Figure 3: OAT15A transonic airfoil ($M = 0.745$, $Re_{/c} = 3.0\ 10^6$, $\alpha = 0.9^o$) - Very fine structured grid - Mach number distribution, stagnation enthalpy and entropy productions.

The theory is based on the assumption that production of viscous drag and wave drag is confined to finite control volumes V_v (boundary layers and viscous shear layers) and V_w (shock layers), and that the flow can be considered as inviscid outside these volumes [4] (see figure 4). If V_v and V_w can be defined without overlap, wave and viscous drag can be expressed as:

$$D_v = \int_{V_v} div\, \vec{f_{vw}} dV \tag{5}$$

$$D_w = \int_{V_w} div\, \vec{f_{vw}} dV \tag{6}$$

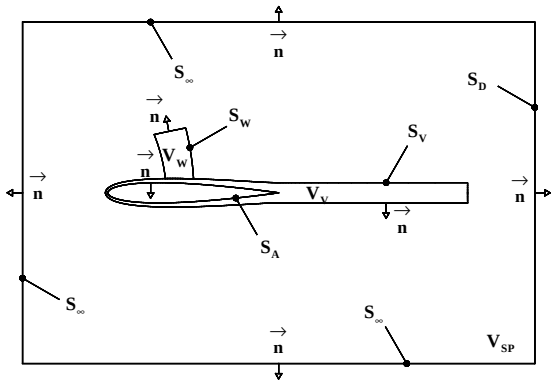

Figure 4: Boundaries and control volumes for far-field drag breakdown.

2.2.2 Lift-induced drag

Lift-induced drag is related to reversible phenomena which involve only exchange of mechanical energy. Transverse kinetic energy is added to the flow downstream of lifting finite surfaces.

For the definition of induced drag, it is convenient to create a third vector $\vec{f}_i$ such that:

$$\vec{f} = \vec{f_{vw}} + \vec{f}_i \tag{7}$$

$$\vec{f}_i = -\rho(u - u_\infty - \Delta\overline{u})\vec{q} - (p - p_\infty)\vec{i} + \vec{\tau_x} \tag{8}$$

The formula proposed by van der Vooren for induced drag [4] in the case of a non-propelled aircraft is:

$$D_i = \int_{V_i} div\vec{f}_i dV - \int_{S_A} (\vec{f}_i.\vec{n})dS \tag{9}$$

It can be shown [4] that in the volume integral, the volume of the computational domain V_i can be theoretically replaced by $(V_v \cup V_w)$, or, if numerical spurious drag sources are present in the field by $(V_v \cup V_w \cup V_{sp})$, where V_{sp} is a volume containing the spurious drag sources.

3 SPURIOUS DRAG PRODUCTIONS

Within the mesh generation step, the continuum of space is replaced by a finite number of points where the aerodynamic variables have to be determined. The accuracy of the numerical approximation is obviously in direct link with the grid refinement and the error of the numerical simulation has to tend to zero when the dicretized space approaches the continuum [15]. For complexe 3D configurations such as aircraft, to ensure a compromise between mesh size and computational costs it is often necessary to limit the number of points and so the grid quality. So, the numerical approximation may deviate slightly from the real flow because of the insufficient discretization in some regions of the grid. This study aims at identifying the effects of the combination mesh discretization-quality / numerical methods on the aerodynamic variables evaluation and to propose a way to increase the reliability of the CFD drag prediction.

3.1 Spurious drag productions: localisation and elimination

Computations of the flow around the AS28 wing / body configuration in transonic cruise conditions ($M_\infty = 0.80$, $Re_{/m} = 11.0\ 10^6$, $CL = 0.50$) with the unstructured DLR-Tau code [11] [10] are discussed in this section.
The main numerical settings used with this finite volume vertex-based solver are the following: Runge-Kutta scheme for time integration, Jameson centred scheme with artificial viscosity for space discretisation, multigrid technique for convergence acceleration and one-equation Spalart-Allmaras model as turbulence model.

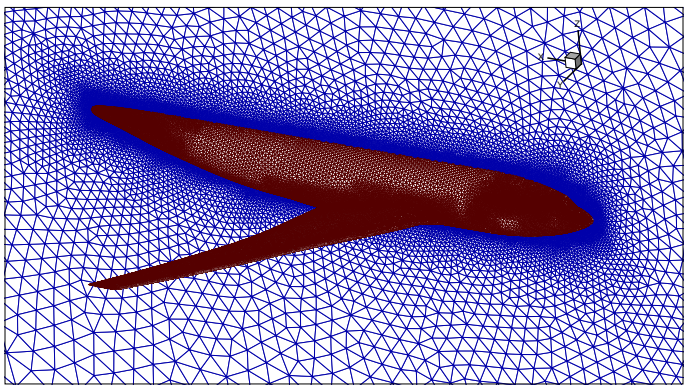

Figure 5: AS28 Wing/Body configuration - Initial hybrid mesh.

The initial unstructured hybrid grid (35 prism layers, about 3 million nodes) (see figure 5) was adapted two times during the computation (refinement sensors based on velocity and total pressure gradients) in order to ensure a high quality grid. To limit the numerical effects the artificial viscosity parameters of the centred Jameson scheme were reduced to low levels during the calculation.

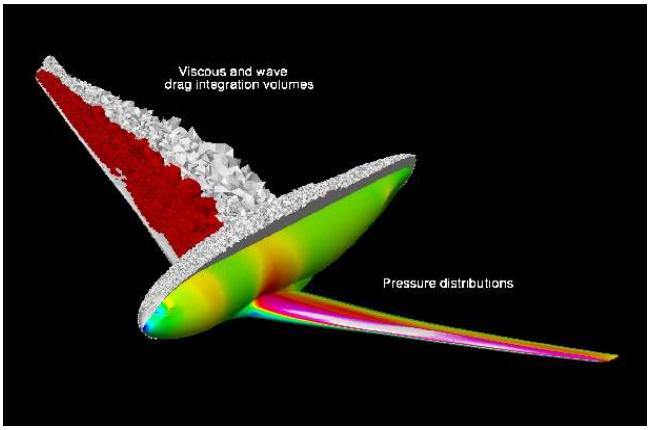

Figure 6: AS28 Wing/Body configuration - Hybrid grid - Pressure distribution and viscous (in grey) and wave (in red) drag integration volumes.

Within the far-field drag extraction process, physical criteria permit to detect the viscous and wave drag productions within the flow field and so to separate the irreversible drag productions created within the shear layers and within the shock region as illustrated in figure 6.
Thanks to its cell-by-cell approach, the drag extraction method allows the visualization of all the irreversible drag sources, spurious as well as physical, throughout the flow field as presented in cyan color in figure 7. The resulting non-selected zones of irreversible drag productions are related to spurious drag (see yellow productions in figure 7). So, numerical effects do not affect the far-field drag values. This is an asset of the method because direct surface force integration given by aerodynamic codes cannot distinguish spurious contributions to drag from physical production, and spurious drag is systematically included in the pressure drag (demonstration in the following section).
For this hybrid RANS computation, the level of spurious drag is limited: 3.1 drag counts (see detailed drag breakdwon in table 1).

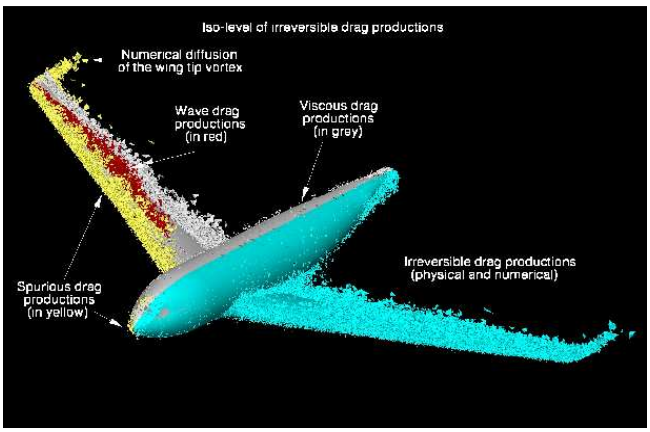

Figure 7: AS28 Wing/Body configuration - Hybrid grid - All irreversible drag sources (in cyan) and separation of physical (viscous drag productions in grey color and wave drag productions in red color) and spurious drag sources (in yellow color).

Figure 7 shows that the spurious drag productions are located around the fuselage nose and the wing leading-edge where the pressure and velocity gradients are very strong and the grid not enough refined. It is also interesting to notice some spurious productions just behind the wingtip coming from the numerical diffusion of the wingtip vortices.

Table 1: AS28 Wing / Body - ($M = 0.80, Re_{/m} = 11.0\ 10^6$) - Drag breakdown.

	CL	CD_p	CD_f	CD_{nf}	CD_w	CD_v	CD_i	CD_{ff}	CD_{sp}
TAU - FFD72	0.500	157.8	89.4	**247.2**	16.5	132.5	95.1	**244.1**	3.1

For computational costs purposes and/or for more complex configurations, it is not always possible to generate high quality meshes and so the numerical error may become penalizing for the drag prediction. In the next section, we will show the effect of spurious drag productions on the pressure drag component firstly on a simple Euler case and secondly on a wing-body configuration in RANS simulation while showing that the far-field drag extraction method can predict the far-field drag component with high reliability.

3.2 Spurious drag productions: over-estimation of pressure drag

For the sake of this demonstration, we consider firstly a simple inviscid calculation which is not representative of industrial practices but which provides a direct insight within the concept of spurious drag productions in link with surface discretization / mesh quality and its impact on the pressure drag values. Secondly a RANS computation on a wing / body configuration allows to isolate the influence of the mesh quality with the objective of a reliable drag extraction.

3.2.1 Inviscid calculation on NACA0012 airfoil

Inviscid calculations on three different two-dimensional structured meshes of increasing refinement: coarse (257x33), medium (513x65) and fine (1025x129) on the symmetrical NACA0012 airfoil (see figure 8) are presented in this section.

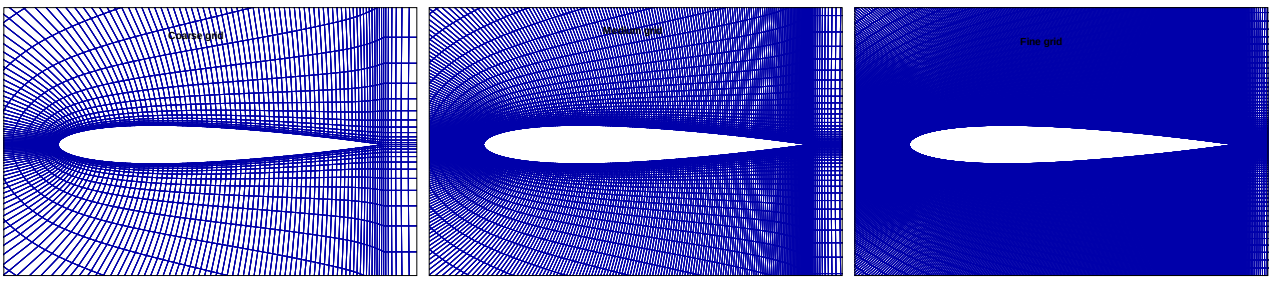

Figure 8: NACA 0012 - Coarse, medium and fine structured grids.

The calculations are performed in inviscid transonic conditions: Mach number $M_\infty = 0.77$ and $\alpha = 0.0^o$ with the ONERA-elsA code.
The object-oriented software elsA [12] [13] uses a cell-centered finite-volume discretization on structured multi-block meshes. For the structured computations presented in this paper the time integration is carried out by a backward-euler scheme with implicit LU-SSOR relaxation, the spatial discretisation is realised through a central Jameson scheme with artificial viscosity. The multigrid technique is used to accelerate the convergence.

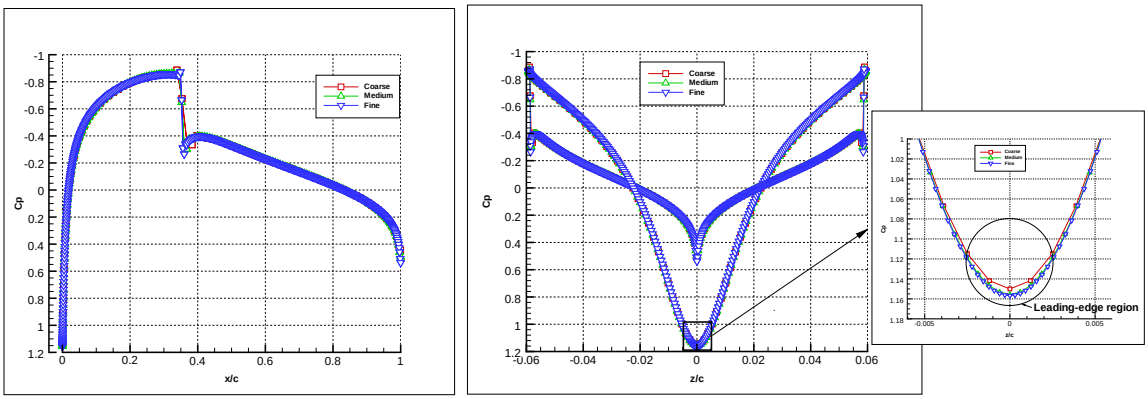

Figure 9: NACA 0012 (Euler, $M_\infty = 0.77$ and $\alpha = 0.0^o$) - Cp distribution.

The pressure distributions obtained with the 3 different grids (see figure 9) exhibit an overall satisfying agreement. We can only notice that the coarse mesh is not enough refined to capture the schock correctly, indeed it appears on several cells on the pressure distribution. But when zooming on the leading-edge region which is a zone of very high pressure gradients a non negligible scatter is visible on the Cp values. With the coarse grid, the mesh discretization near the stagnation point is insufficient to determine very accurately the pressure distribution, in particular the pressure peak level. Furthermore, the facets near the leading-edge have a big impact on the drag but not on the lift because of their outward normal directions which are almost parallel to the free-stream direction. This very local pressure errors have a non-negligible impact on the pressure drag value because the equilibrium between the front and rear part of the airfoil is slighty modified. As a consequence in this case, the pressure drag exhibits large drag variations i.e. 4.3 drag counts between the coarse and the fine grid (details in table 2).

Table 2: NACA 0012 (Euler, $M_\infty = 0.77$, $\alpha = 0.0^o$) - Structured grids - Pressure drag, wave drag and spurious drag values.

	CD_p	CD_w	CD_{sp}
Coarse	13.2	9.4	3.8
Medium	9.6	8.8	0.8
Fine	8.9	8.8	0.1

Figure 10 shows the sum of all the irreversible drag productions (physical as well as spurious) in the streamwise direction. Some numerical perturbations appear clearly around the leading-edge coming from production-destruction of drag in this region. The lower the grid refinement the higher the intensity of this phenomena as confirmed in black lines in figure 11 where spurious drag productions can be localized near the leading-edge and also near the trailing-edge.
The shock wave physical sensor used within the far-field drag extraction process permits to select only the irreversible drag productions coming from the physical shock wave. So, the spurious drag productions generated outside the shock region are implicitly excluded from the far-field drag breakdown (only wave drag in this 2D inviscid transonic computation). Table 2 summarizes the wave drag values obtained with the three grids: the prediction is reliable with medium and fine grids while the coarse grid is too large to ensure a correct flow simulation. However, it is interesting to notice the drag scatter between the three configurations: 0.6 drag counts on the wave drag against 4.3 pressure drag counts between the coarse and fine computations.
The level of spurious drag is very important for the coarse computation (3.8 drag counts), limited for the medium calculation (0.8 drag counts) and almost zero for the fine grid.

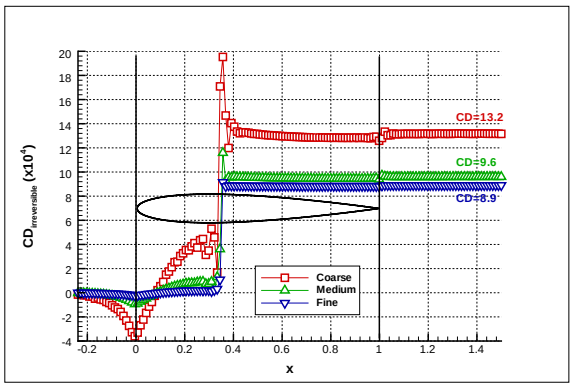

Figure 10: NACA 0012 (Euler, $M_\infty = 0.77,\ \alpha = 0.0^o$) - Streamwise sum of all the irreversible drag productions.

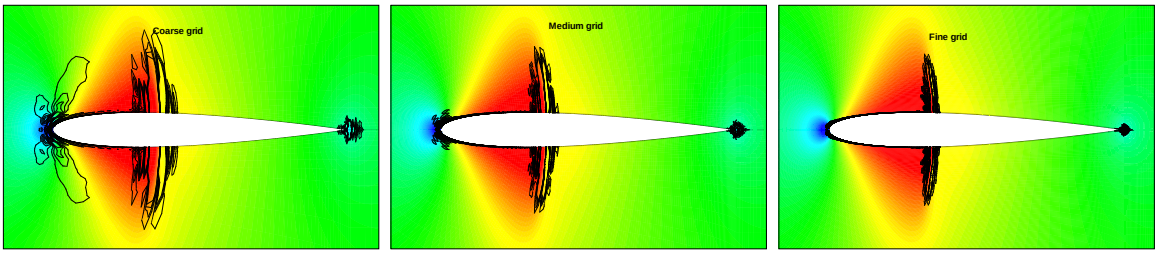

Figure 11: NACA 0012 (Euler, $M_\infty = 0.77,\ \alpha = 0.0^o$) - Structured grids - Mach distribution and irreversible drag production (physical and spurious).

In this case, we can identify **two main sources for the spurious entropy productions: insufficient surface discretization and also too poor mesh refinement around the configuration.** The elimination of the spurious productions with the far-field approcach leads to very reliable drag prediction for the medium and fine calculations

The next test case presents the influence of mesh refinement on the spurious entropy productions within the flow-field and on the pressure drag value with an identical surface discretization on the configuration.

3.2.2 Viscous flow on transonic wing body configuration

The AS28 wing / body configuration is here computed in cruise conditions with the structured ONERA-elsA code as in the previous airfoil case.
For this demonstration, a comparison is made between a structured fine mesh and a Patched Grid mesh generated on the basis of this fine one by using partially coincident frontiers (see meshes around the fuselage nose in figure 12). This technique allows to keep a very good refinement in the viscous layers, shock areas, wingtip vortices, and permits to reduce the number of points in the far-field (about 33% points saved in this case).
The near-field and far-field drag values are presented in table 3. The near-field drag value is higher (9.2 drag counts) in the Patched-Grid case than in the fine one because of an overprediction of the pressure drag. The far-field drag breakdown shows different levels of spurious drag for each calculation: 5.1 drag counts in the fine case and 17.1 in the Patched Grid case.
Thanks to the spurious drag separation, the far-field drag values obtained on the two solutions are in better agreement than the near-field drag values. Although Patched Grid is a particular kind of multi-block structured mesh, we can conclude here, again, that the quality of the mesh has a greater impact on the near-drag values than on the far-field drag values.

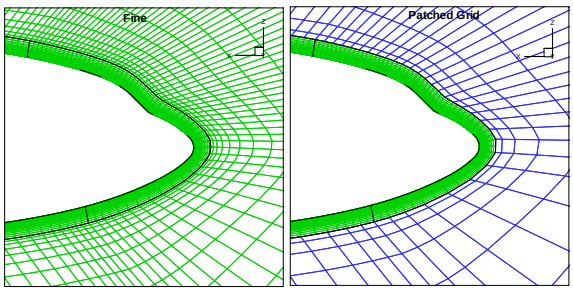

Figure 12: AS28 Wing / Body configuration - Structured coincident and Patched Grid meshes - Spurious drag productions around the nose-fuselage

Table 3: Near-field and far-field drag values.

	CL	CD_p	CD_f	$CD_p + CD_f$
Fine	0.549	194.3	96.6	290.9
PG	0.547	203.5	96.4	299.9

	CD_w	CD_v	CD_i	CD_{ffd}	CD_{sp}
Fine	26.0	149.7	110.1	285.8	5.1
PG	25.0	150.0	107.9	282.9	17.1

An exhaustive analysis of the field exhibits a larger non-physical entropy creation (spurious drag productions) around the fuselage nose in the Patched Grid case than in the fine one as shown in figure 13.

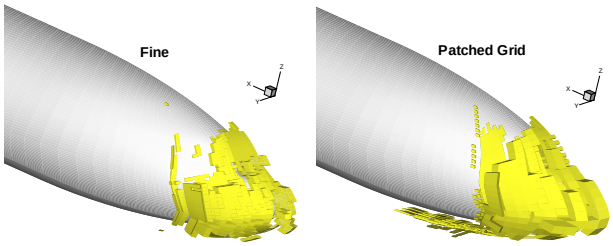

Figure 13: AS28 Wing / Body configuration - Structured coincident and Patched Grid meshes - Spurious drag productions around the fuselage nose

The top illustration in figure 14 presents the evolution of the friction and pressure drag when progressively added on each aircraft surface panel. This clearly demonstrates that no difference, between the two solutions, appears for the friction drag at the skin of the configuration but concerning the pressure drag: panels 5, 6 and 7 are responsible of 6 pressure drag counts of over-estimation while panels 8 to 12 produce 3 drag counts more in the Patched Grid case than in the fine one (see bottom graph in figure 14). So the pressure drag, is in close link with the quality of the mesh.
In this case, the brutal change in cell sizes around the fuselage nose which is a region of high velocity gradients (although in "inviscid region" because outside the boundary layer) is responsible of large spurious drag productions.
In the general case, the spurious productions are located around the stagnation points (leading edge, fuselage nose, nacelle lips, ...), where the pressure gradients are very high and the meshes not enough refined in these large curvature zones. As a consequence, the surface pressure exerted on the body is modified

and the equilibrium between the front and the back parts of the configuration is slightly changed leading to different pressure drag values on solutions obtained with different grids for a same configuration.

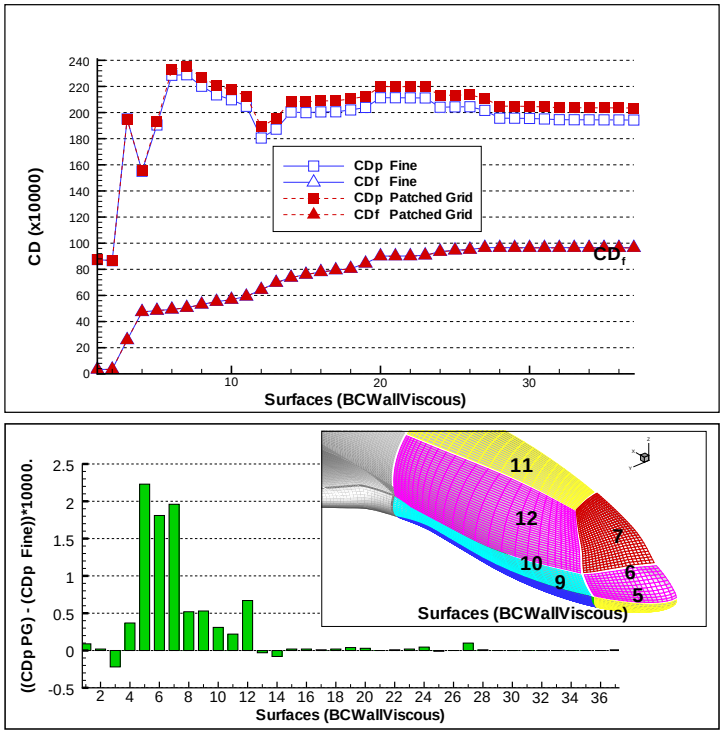

Figure 14: AS28 wing / body configuration - Structured coincident and Patched Grid meshes - Identification of over-estimation of pressure drag

This demonstration points out the importance of the mesh quality in the drag extraction process and confirms that **for an accurate resolution it is necessary to ensure an excellent refinement in all the complex parts of the flow, not only in zones containing physical phenomena which generate drag but, also in inviscid high gradient regions.**
So within the whole drag extraction process, it is necessary to generate a good quality initial mesh for the structured approach (because mesh adaptations are not very widespread in structured cases) and to use the mesh adaptation procedure to improve the grid quality in the unstructured case, even if, thanks to the far-field drag method the sensitivity to the mesh quality is largely reduced because of spurious drag elimination.

3.3 Spurious phenomena: numerical diffusion of wingtip vortices

In lifting flow problems, the wingtip vortices created when the flow tends to curl around the wingtip from bottom high-pressure region to top low-pressure surface must be convected by the main flow [17] behind the configuration on long distances. These vortices are regions with low-pressure area in the center surrounded by fast transverse velocities. They are generated through a reversible phenomenon which involves only an exchange of mechanical energy and generates an extra pressure imbalance on the surface of the wing responsible of the called lift-induced drag, which is the price to pay to achieve lift on an airplane.
In CFD simulations, the transverse kinetic energy decreases downstream of the body at a much faster rate than in reality because of numerical diffusion of the wingtip vortices [18] [19]. Indeed, the insufficient mesh refinement and the artificial dissipation contained in numerical schemes lead to the conversion of a part of the lift-induced drag into spurious viscous drag. This is what we call the spurious decay of trailing vorticity.

Figure 15 represents the irreversible drag productions, physical as well as spurious, which develop around a representative aircraft configuration in cruise conditions: the AS28 wing / body configuration computed with the ONERA-elsA multi-block structured code in transonic conditons ($M_\infty = 0.80$, $Re_{/m} = 11.0\ 10^6$, $CL = 0.50$). This figure allows to visualize all the irreversible drag productions coming respectively from physical phenomena such as boundary and shear layers as well as shock wave, due to spurious effects at wing leading-edge and also from the numerical diffusion of the wingtip vortices.

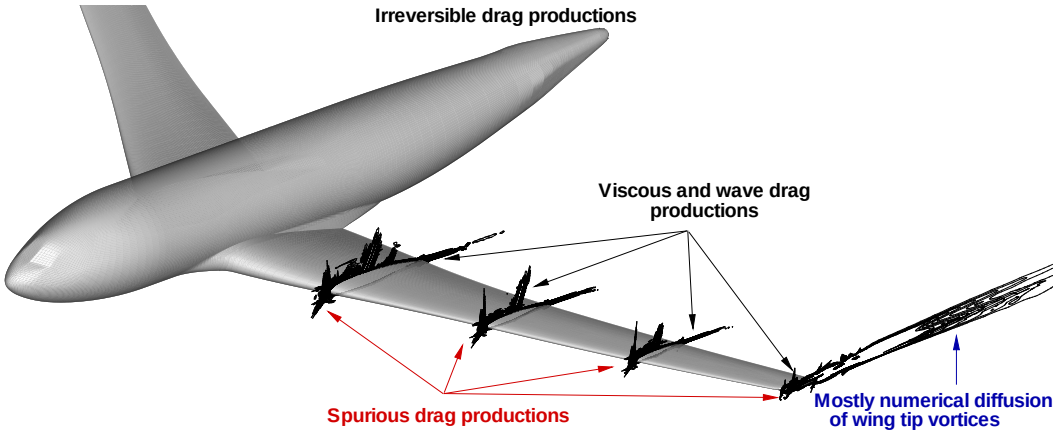

Figure 15: AS28 Wing / Body configuration - Structured computation - Irreversible drag productions in spanwise sections.

As indicated above, lift-induced drag comes from an exchange of mechanical energy which should not imply irreversible transformations outside the physical viscous vortex core (core size around 2% of the vortex diameter on large aircraft). But in CFD, the numerical development of the trailing vortices, or more precisley its convection by the main flow, deviates from the real physics because of predominant numerical effects. This is illustrated in figure 16 where red and blue colours visible on the streamlines crossing the wingtip vortex indicate spurious entropy variations in these regions.

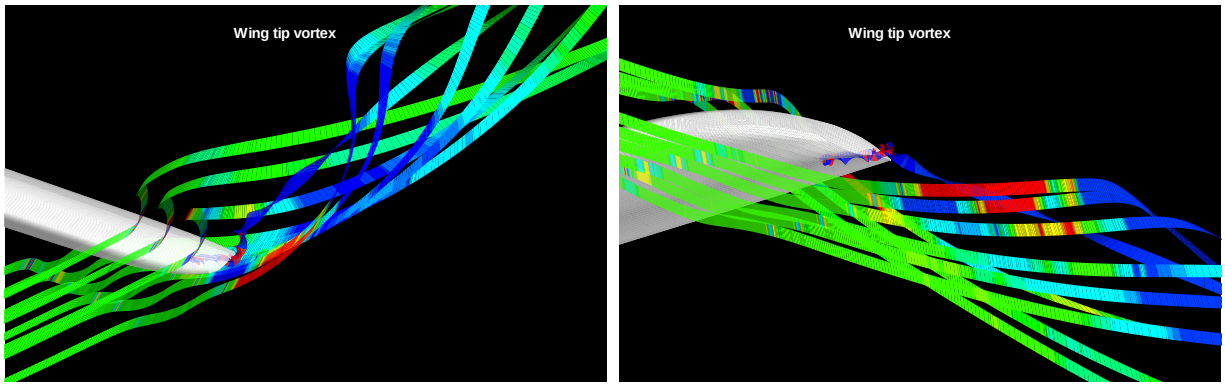

Figure 16: AS28 Wing / Body configuration - Structured computation - Streamlines crossing the wingtip vortex where red and blue colours indicate spurious entropy variations.

For this structured computation, the amount of irreversible drag coming from the numerical diffusion of the wingtip vortices (integrated from the wingtip to a given x-station in a volume embedding the curling vortices) is limited: only 3 drag counts at a half fuselage length behind the wingtip (see figure 17).

To ensure an accurate lift-induced drag prediction, this numerical error must be added to the called "apparent lift-induced drag" obtained with formula 9 which, at a sufficient downstream distance, is approximated by an integral of the transverse kinetic energy. This correction ensures a reliable lift-induced drag prediction almost independent on the downstream extend of the integration volume (see the corrected lift-induced drag curve in figure 17). So the numerical error is totally corrected with the far-field approach.
Remark: in unstructured computations (especially with tetrahedral elements), the numerical diffusion may be so intense that vortices may disappear totally only a few fuselage length behind the aircraft.

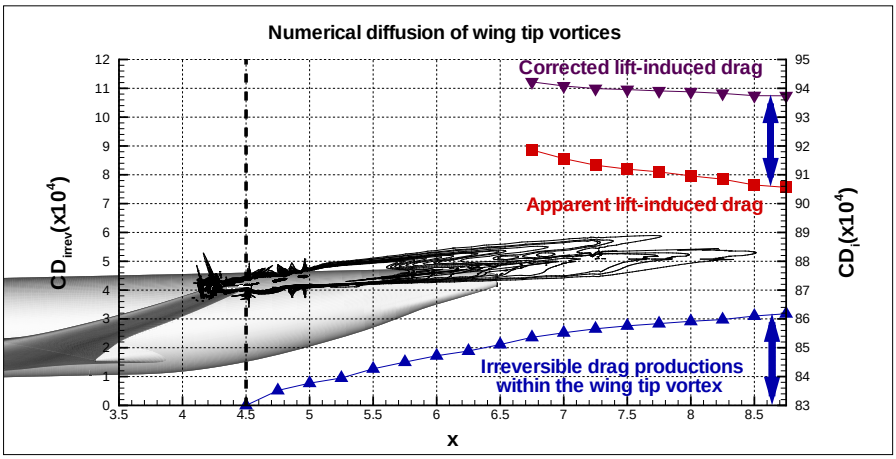

Figure 17: AS28 Wing / Body configuration - Structured computation - Numerical diffusion of wingtip vortices and correction of lift-induced drag computation.

The physical phenomenon, trailing vorticity, is correctly captured at the wingtip but the corresponding crossflow kinetic energy decreases at a much faster rate than in reality because of numerical error, this causes the conversion of a part of the lift-induced drag into irreversible drag through purely numerical effects. It appears that, in a first time the curling action is well modelized by CFD (ensuring a correct pressure drag prediction with the direct near-field method), but in a second time the combination discretized space / numerical methods does not permit to convect without losses the wingtip vortices in the far-field, and as a consequence its evolution deviates from the one observed in real flows.
This numerical diffusion may be very penalizing for example to compute accurately the wake vortices for aircraft distance separation prediction or also to simulate efficiently the blade / vortex interaction for helicopter applications.
But concerning the drag prediction, it is important to notice that the spurious decay of the transverse kinetic energy has no impact on the near-field drag although this component is strictly a pressure drag. This is due to the conversion of a form of drag (lift-induced drag) into another form (spurious viscous drag) because of numerical errors and not a "pure" spurious creation outside drag production zones as it was the case for example for the spurious drag productions around the stagnation line as presented previously.

The numerical diffusion of wingtip vortices modifies the flow variables in the curling region but has no impact neither on the near-field drag (without any correction), nor on the far-field drag because the correction matches exactly the numerical error.

3.4 Remark: spurious drag as mesh adaptation sensor

A mesh adaptation strategy based on an irreversible drag sensor would lead to an intelligent and efficient grid refinement, as tested by Yamazaki [20], because all the insufficiently refined zones would be enriched.

The zones of physical drag productions (boundary and shear layers, shock regions) as well as the regions of spurious drag productions would be thereby better discretized leading to more accurate numerical solutions. So, this strategy would allow to reduce the spurious drag level in CFD results by limiting the number of points for affordable computational costs.

4 CONCLUSION

This study has shown that the numerical error introduced in CFD solutions because of the space discretisation and numerical methods has a non negligeble impact on the near-field drag components especially on the pressure drag, but is largely reduced with the far-field approach.
The far-field drag extraction method which implies the analysis of numerical as well as physical phenomena allows to eliminate the spurious drag productions for an accurate and reliable drag prediction.
Furthermore, the evaluation of the physical components of drag and the localisation of the sources of viscous and wave drag provide very useful and rich information in aerodynamic analysis and design.
The evaluation of the lift-induced drag component also affected by a spurious phenomena is efficiently corrected.
The far-field drag method permits to assess the computational uncertainty, no matter the meshing strategy (structured or unstructured) and the numerical techniques used for the CFD simulation, the spurious drag level gives a confident measure of the error committed through the aerodynamic assessment process.
Thanks to the localisation of spurious drag productions, the post-processing method gives an issue to improve the mesh quality for a more accurate CFD computation and thanks to the elimination of spurious drag ensures a reliable drag extraction from numerical solutions.

Acknowledgments

The author would like to thank D. Destarac for his very helpful advice.

References

[1] J.W. Slooff, *Computational Drag Analysis and Minimization (Mission Impossible ?),* AGARD-R-723, 1985.

[2] A. Rizzi, *Spurious Entropy Production and Very Accurate Solutions to the Euler Equations,* The Aeronautical Journal, 1985.

[3] J. van der Vooren and J.W Slooff, *CFD-Based Drag Prediction; State of the Art, Theory, Prospects,* NLR, Technical Publication, TP 90247 L, 1990.

[4] J. van der Vooren and D.Destarac, *Drag / Thrust Analysis of Jet-propelled Transonic Transport Aircraft; Definition of Physical Drag Components,* Aerospace Science and Technology Vol.8, N^o7, October 2004.

[5] D. Destarac, *Far-Field / Near-Field Drag Balance Applications of Drag Extraction in CFD,* VKI Lecture Series 2003, CFD-based Aircraft Drag Prediction and Reduction, National Institute of Aerospace, Hampton (VA), November 3-7, 2003.

[6] M.R. Mendenhall, R.E. Childs and J.H. Morrison, *Best Practices for Reduction of Uncertainty in CFD Results (Invited),* AIAA 2003-0411, January 2003.

[7] R.E. Childs, *Error and Uncertainty Estimation in CFD ,* NEAR TR 574, Nielsen Engineering and Research, Muntain View, CA May 2002.

[8] M. B. Giles and N. A. Pierce, *Adjoint Error Correction for Integral Outputs,* Oxford Univeristy, September 2001.

[9] A. Barthet, C. Airiau, M. Braza and L. Tourette, *Adjoint-Based Error Correction Applied to Far-Field Drag Breakdown on Structured Grids,* AIAA Paper 2006-3315, San-Francisco, California, June 2006.

[10] S. Melber-Wilkending, R.Wilhelm and H.F. von Geyr, *RANS Solutions for a Complex High-Lift Configuration of a Transport Aircraft with Engine Including Improved Resolution of the Nearfield,* AIAA, 2004-5081, 2004.

[11] R. Schawmvorn, T.Gerhold and Ralf Heinrich, *The DLR TAU-Code: Recent Applications in Research and Industry.* ECCOMAS CFD 2006, Netherlands, 2006.

[12] L. Cambier and M.Gazaix, *elsA: An Efficient Object-Oriented Solution to CFD Complexity.* AIAA 2002-0108, Reno, Jan.2002.

[13] M. Gazaix, A.Jolles and M.Lazareff, *The elsA Object-Oriented Computational Tool for Industrial Applications.* ICAS Congress, 2002.

[14] S. Esquieu, *Aircraft Drag Extraction from Patched Grid Computations,* 21st AIAA Applied Aerodynamics Conference, Orlando (USA), AIAA-2003-3659, June 23-26, 2003.

[15] C. Hirsch, *Numerical Computation of Internal and External Flows,* Volume 1, Fundamentals of Numerical Discretization, Wiley and Sons, 2001.

[16] S. Esquieu, M. Méheut, H.F. von Geyr, O. Brodersen, *Far-Field Drag Extraction from Numerical Solutions and Wake Surveys,* 7th ONERA-DLR Aerospace Symposium, Toulouse, France, 4-6 October 2006.

[17] J.D. Anderson, *The Airplane: A History of Its Technology,* December 2002.

[18] D. Destarac, *Drag Extraction from Solutions of the Euler and Navier-Stokes Equations,* Extended Abstract, 1st ONERA-DLR Aerospace Symposium, Paris, France, 1999.

[19] R.M. Cummings, M.B.Giles and G.N.Shrinivas, *Analysis of the Elements of Drag in Three-Dimensional Viscous and Inviscid Flows.* AIAA Paper 96-2482, 1996.

[20] W. Yamazaki, *Study of Advanced Aerodynamic Analysis and Shape Optimization Using Drag Decomposition Method,* PhD Thesis, Tohoku University, 16 January 2007.